Faculty of Engineering Science,
The University of Western Ontario,
London, Ontario. N6A 5B9.

Studies Relating to Meteor-Burst Communications Systems.

A. R. Webster, J. Jones, K. J. Ellis and P. G. Brown.

scientific Authority. Sherman Chow

Final Report,
S.S.C. Contract 36001-2-3536/01-ST
March, 1993.

Studies Relating to

Meteor-Burst Communications Systems

A Final Report under

Supply and Services Canada

Contract # 36001-2-3536/01-ST

submitted to

Department of Communications,

Communications Research Centre,

Ottawa, Ontario.

Pricipal Investigator: A. R. Webster.

Co-Investigator: J. Jones.

Research Associates: K. J. Ellis,

P. G. Brown.

March, 1993.

Table of Contents.

1. Introduction.

This report deals with a second phase of meteor-burst comunications studies following on from the development of an angle-of-arrival system designed to provide a measure of the distribution of the positions of suitable meteors in a forward-scatter system (see Webster et al, 1992). Results reported so far from that study, which used a 600 km path, Ottawa-Elginfield, indicate clear diurnal and seasonal effects and preferred directions, as was broadly expected. The operation of such a forward scatter system as a communications link would be very dependent on the distribution of meteor radiants and these kind of statistics. Of some importance is the ability to predict the performance of such systems in different locations and with different path lengths and orientations.

The objective of the work described here is two-fold. First, the prediction of meteor rates on the general forward-scatter system is investigated with an eye on the likely effects of the observed radiant distribution of sporadic (the most common) meteors. In order to address this problem, a survey of the results from many different observational techniques has been used to arrive at a radiant distribution and a technique has been developed to predict the expected echo rates from this. An initial test of this approach is carried out using the Ottawa-Elginfield link and the result compared with the experimentally obtained data.

The second part is concerned with the transfer function of a typical meteor burst communications system, and the objective was to design equipment to measure this. Reasonable simplicity of operation and concurrent use with the existing forward-scatter system were used as guidelines. Several alternative approaches were examined and discussed with C.R.C. personnel, all based on wide-band measurments. Very much as a cooperative venture between C.R.C. and U.W.O., a system based on the CHIRP principle was settled upon, utilizing some already existing equipment, and a detailed design has been completed. The expectation is that simultaneous measurements using both systems will take place in the near future.

2. Predicting the echo rate

Our ultimate goal is to be able to predict the performance of any meteor burst system at any location at any time of day or year. One important aspect of such a prediction is the rate of meteor burst events that are suitable for the transmission of information. In general, the rate of echoes is determined by both the flux of meteoroids and by the ability of the communication system to detect echoes from the meteor trains produced by these meteoroids as they ablate in the Earth's atmosphere. Mathematically, this can be expressed in the form

$$\Xi(t)=\iint\Phi(\alpha,\delta)\ \Theta(\alpha,\delta,t)\ d\alpha\ d\delta \tag{2.1}$$

where $\Xi(t)$ is the echo rate as a function of time, $\Theta(\alpha,\delta,t)$ is the flux of meteors from the radiant at the celestial coordinates α and δ, and $\Phi(\alpha,\delta)$ is a function describing the effective collecting area of the system to meteors from the radiant point (α,δ). In the following sections we describe our attempts to determine the functions Φ and Θ.

It is an impossible task to deconvolve the meteoroid flux distribution from the effective collecting area function by analyzing the echo rates from a single meteor radar or a single forward-scatter meteor burst system. If one of either Φ or Θ is known then it is possible to determine the other. We first discuss the calculation of the effective collection area and then address the problem of the determination of the meteoroid flux distribution.

The calculation of the effective collecting area is an involved procedure for which there has been no general algorithm available which bridges the complete gamut from back-scatter meteor radars to meteor burst forward-scatter systems. We have devised such a method and applied it our short-hop forward-scatter system for which none of the standard methods are appropriate.

In principle it is possible, given the location of the sporadic meteor sources, to use a least-square fitting procedure to determine both the widths of the sources and their strengths but because the of the non-linear nature of the problem this is a very difficult task. A simpler undertaking is to take the widths of the sources as revealed by the various meteor orbit surveys and to limit the least-squares fit to the determination of the source strengths. But although this is straight-forward, it nevertheless involves a great deal of effort and in the meantime we content ourselves with a comparison of the observed echo rates over the year with the predictions of one arbitrary but fairly realistic radiant model.

2.1 The effective collecting area function, Φ.

The ground work for the theory of the response of forward-scatter meteor burst systems was laid by Hines (1955) who first discussed the case of a widely spaced transmitter and receiver which allowed him to make simplifying assumptions concerning the system geometry. He later extended his theory (Hines, 1958) to much closer transmitter-receiver spacing but his description of the methods he used were so scant that it was difficult to duplicate them. In the present treatment we have derived an independent procedure which is based on the approach taken by Kaiser (1960) for use with back-scatter meteor radars. We try to describe our method as clearly as possible to make it useful for other workers.

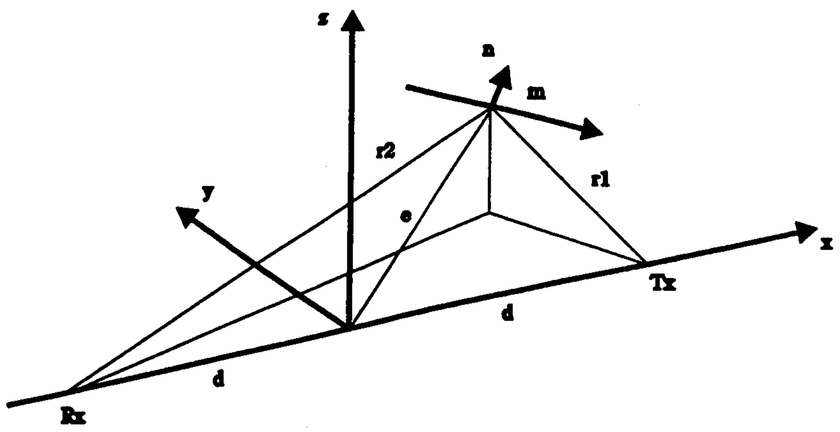

Figure 2.1 The forward-scatter reflection geometry.

As can be seen from figure 2.1 above, the vector in the direction of the meteor radiant is m, so that the condition for specular reflection is

$$m \cdot n = 0, \tag{2.2}$$

where n, the normal to the train is given in terms of the vectors $\mathbf{r}_1$ and $\mathbf{r}_2$ from the transmitter and receiver by

$$n = \frac{r_1}{|r_1|} + \frac{r_2}{|r_2|}. \tag{2.3}$$

Since meteors ablate in a fairly narrow height range close to 100 km, we can regard the echoes as coming from points on an "echo surface" and we therefore set z=1.0 and work in terms of a unit of length of 100 km. The locus of points satisfying the specular condition is a line on the echo surface for which it is difficult to find an analytic expression. Hines(1958) gives an alternative derivation of the specular condition but provides no insight into the method he used to derive the echo lines and we consider likely that he used graphical methods which do not lend themselves to a general numerical solution of the problem.

Taking

$$m=\begin{pmatrix} a \\ b \\ c \end{pmatrix}, \qquad e=\begin{pmatrix} x \\ y \\ z \end{pmatrix} \tag{2.4}$$

it is straightforward but tedious, to show that the slope of the echo-line, *dy/dx*, on the echo surface is given by

$$\frac{dy}{dx} = \frac{f_1\, h_1 + f_2\, h_2}{g_1\, h_1 + g_2\, h_2} \tag{2.5}$$

where

$$\begin{aligned}
f_1 &= 2ax^2 = x(by-2ad+c)+ay^2-bdy+a-c) \\
f_2 &= 2ax^2+x(by+2ad+c+ay^2+bdy+a+cd) \\
g_1 &= bx^2+x(ay-2bd)+2by^2+y(ad+c)+b(d^2+1) \\
g_2 &= bx^2+x(ay+2bd)=2by^2+y(c-ad)+b(d^2+1) \\
h_1 &= \sqrt{x^2+2dx+y^2+d^2+1} \\
h_2 &= \sqrt{x^2-2dx+y^2+d^2+1}
\end{aligned} \tag{2.6}$$

If we can find one point on the echo-line, we can determine the rest of it by integrating along it using the above equations. We found it convenient to force the starting point to be at a distance of 10 units from the mid-point of the system (1000 km) and determined its precise location by applying Newton's root-finding method to equation (2.2) .

To illustrate the results given by this procedure we have calculated the echo-lines for two sets of radiant vectors: the first in the *x-z* plane and the second in the *y-z* plane. The separation of transmitter and receiver was taken as 500 km (d=2.5) as is the case for the Ottawa-London meteor scatter circuit. The results of these calculations are shown in figures 2.2a and 2.2b.

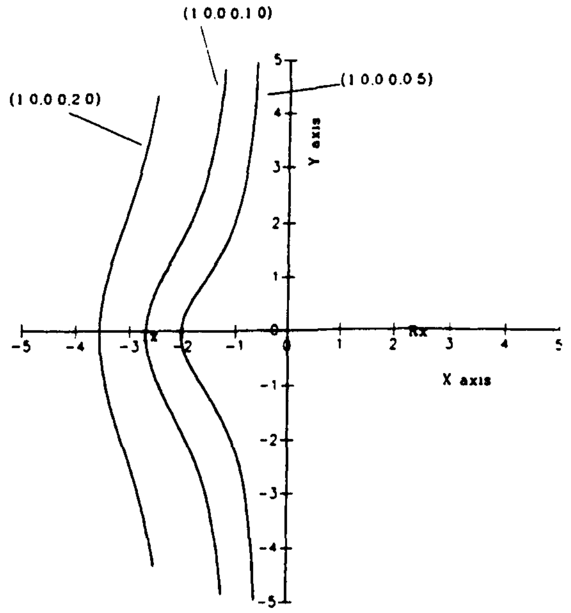

Figure 2.2a Echo-lines for several radiants in the y-z plane for the Ottawa-London forward-scatter circuit.

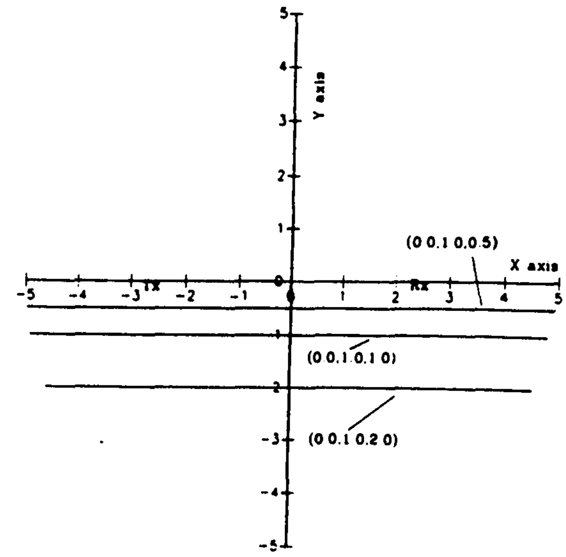

Figure 2.2b Echo-lines for several radiants in the y-z plane for the Ottawa-London forward-scatter circuit

Although we have so far assumed all the meteoroids to ablate at the same altitude, meteor trains extend over a vertical height range of several kilometres so that the echo lines are in fact broadened into what we might call "echo-strips". An important step in the prediction of the echo rate is to determine the effective collecting area of these echo-strips. The essential geometry of the situation is shown below in figure 2.3 and it is readily seen that the area of a small element of the echo-strip, dS, is given by

$$dS = \frac{dh}{n_z}\, k \times n \; dl \tag{2.7}$$

where dh is the mean detectable length of a meteor train.

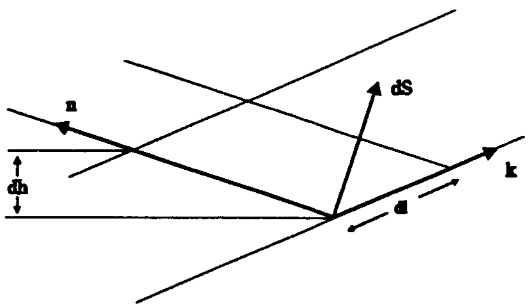

Figure 2.3 The geometry of the various vectors involved in the calculation of the elemental area dS on the echo-strip.

2.1.1 The mean vertical train length

It is clearly important to have a reliable estimate for the mean vertical train length. Since there are few observational data on the ionization profiles of meteor trains, previous studies have assumed the ionization profile to be the same as the rate of mass loss predicted by the classical ablation theory (Kaiser, 1960). Since there is much evidence that the ablation mechanism is much more complicated than the classical theory assumes, we have assumed that the ionization profile is probably similar to the light curves determined by low-light-level TV meteor studies for meteoroids of masses similar to those of radio-meteors. The most recent of such studies is that of Flemming, Hawkes and Jones (1992) who provide the vertical trail length, L, versus the maximum meteor luminosity.

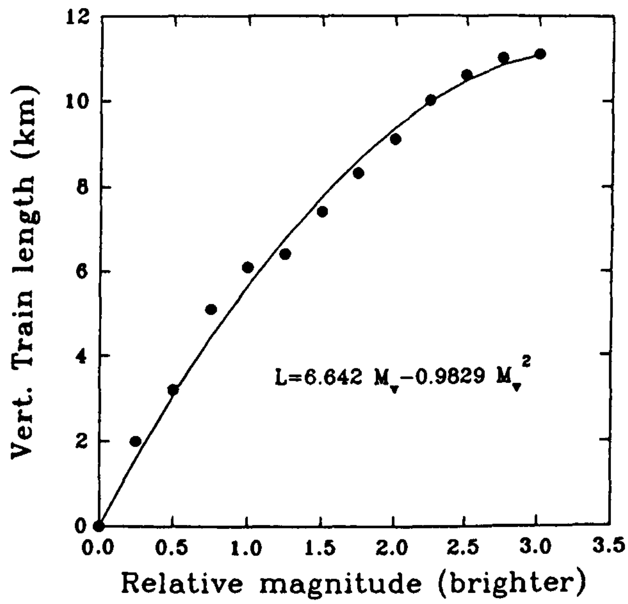

Figure 2.4 The vertical length of TV meteors for which the luminosity is great than ΔM_V below the maximum luminosity of the train.

Their results are shown in figure 2.4 above are well approximated by the empirical formula

$$L = 6.642\ \Delta M_V - 0.9829\ \Delta M_V^2 \tag{2.8}$$

The quantity ΔM is measure of how much brighter the meteor is than the background luminosity I_0 and is given by

$$\Delta M_V = 2.5\ \log_{10}(I_{max}/I_0) \tag{2.9}$$

To find the mean vertical height interval, <dh>, over which the meteor is detectable we need the amplitude distribution of the echoes. In practice, it is found that amplitude distribution is well represented by an equation of the form

$$dn \sim A^{-s} dA \tag{2.10}$$

The mass distribution index, s, is usually in the range 1.5 to 3. The mean vertical train length, <dh>, is given by

$$<dh> = \int_{A_0}^{\infty} L(A)\ A^{-s}\ dA \ / \int_{A_0}^{\infty} A^{-s}\ dA \tag{2.11}$$

where A_0 is the minimum detectable echo amplitude. Since the sensitivity of our forward-scatter system is such that most of the echoes are from underdense meteor trains, the echo amplitude is proportional to the ionization at the refection point which is in turn proportional to the luminosity and this yields the variation of <dh> with s shown in figure 2.5 below.

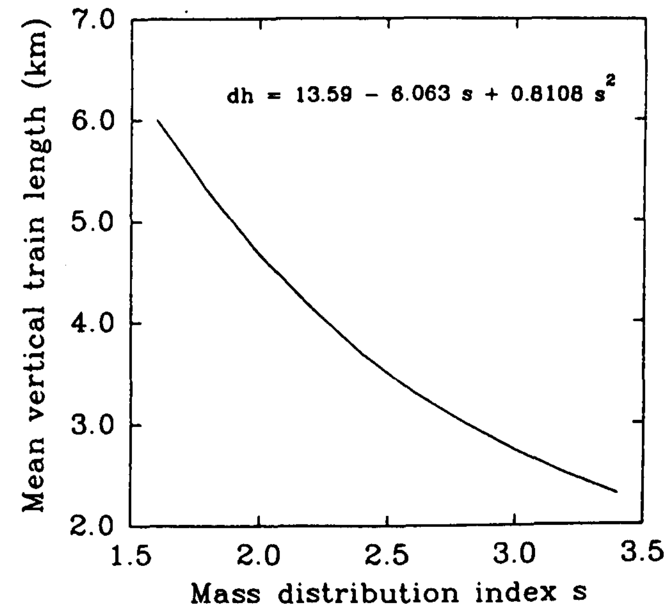

Figure 2.5 The variation of the mean vertical length over which the meteor is detectable as a function of the mass distribution index s.

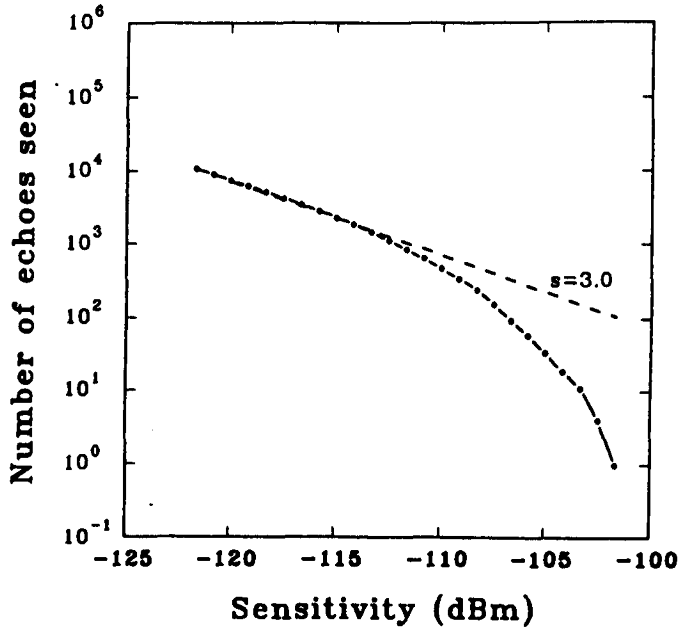

Figure 2.6. The observed amplitude distribution of echoes form the Ottawa-London forward-scatter circuit.

Finally in figure 2.6 above, we show the observed amplitude distribution of the echoes observed on the Ottawa-London forward-scatter circuit and note that s in this case is close to 3.0 which yields a mean vertical train length of 2.73 km.

2.1.2 The system sensitivity function.

The sensitivity of the system varies over the echo surface because of the anisotropy of the antenna gain and variation of range. Since, according to figure 2.6, the majority of echoes are underdense the received echo power, P_R is given by (McKinley, 1961)

$$P_R = \frac{q^2\, P_T\, G_R G_T\, \sigma_e\, \sin^2\gamma}{64\pi^3\, R_1 R_2} \tag{2.12}$$

The $\sin^2\gamma$ term allows for the polarization loss arising from the skewness of the electric vectors at the echoing point. The gain function G_R and G_T are identical in form being the product of dipole, ground and reflector terms.

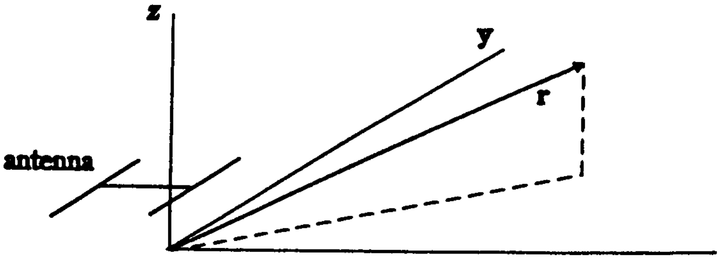

Figure 2.7. Antenna geometry.

Referring to figure 2.7 above, in which **x**,**y** and **z** are unit vectors, the total expression for the gain in the direction of the unit vector, **r**, is

$$G(r) = |\, r \times y\, |^2 \cdot 4 \sin^2 (2\pi h r_z \,/\, \lambda) \cdot |\, 1 + r_x\, |^2 \tag{2.13}$$

Assuming an ideal 2-element Yagi with equal currents in both elements phased for maximum gain in the forward direction and zero gain in the back direction. For our forward-scatter system the height, h, of the array was $3\lambda/8$. As well as being dependent on the antennae gains, the received echo power is also a function of the direction of the meteor train through the so-called Fresnel term:

$$F = \lambda R_1 R_2 \,/\, (R_1+R_2)\, (1-\sin^2\phi \cos^2\beta) \tag{2.14}$$

where the angles ϕ and β are specify the orientation of the train with respect to the propagation and tangent planes (see McKinley, 1961 p 238).

With the above equations we can determine the relative sensitivity of the system *Sens(x,y,m)* on the echo-surface for each point along the echo-line. Then, knowing how the echo rate varies with sensitivity, we can integrate along the echo line to find the effective collecting area of the system for any radiant.

$$\Phi(m) = \int r_z^{s-1}\, Sens(x,y,m)^{\,s-1}\; m \cdot ds \tag{2.15}$$

where the integration is taken along the echo-line for a particular meteor radiant m. We have calculated $\Phi(m)$ for our system and the results of these calculations are represented as a contour plot in figure 2.8 below.

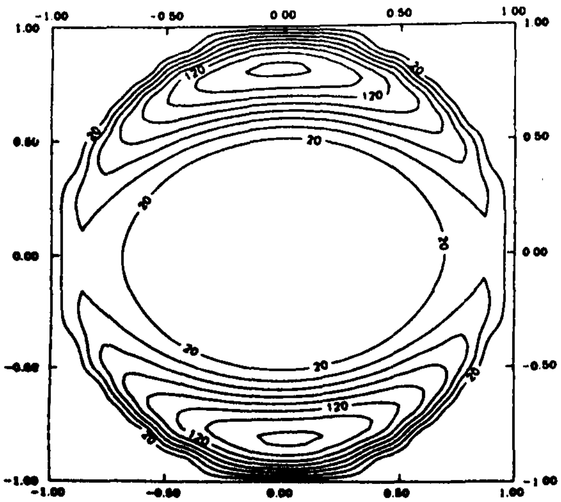

Figure 2.8. The effective collecting area, $\Phi(km^2)$, of the Ottawa-London forward-scatter system. The x and y axes are as shown in figure 2.1 and the coordinates are the components of the unit vector, m, in the direction of the meteor radiant.

2.1.3 The coordinate transformations.

As the Earth rotates about its axis the radiants appear to circle the pole and we therefore need to be able to calculate the position of the radiant with respect to the system coordinates as a function of time. In the celestial system the coordinates, the right ascension and the declination of the radiant, are fixed. To transform them to the system coordinates it is convenient to think of the process in two steps: first to an Earth-based system (east, north,up) and then to the final meteor-burst aligned system (x,y,z).

We first express the celestial coordinates in terms of a cartesian system (u,v,w):

$$\begin{aligned} u&=\sin(\delta) \\ v&=\cos(\delta)\ \cos(ha) \\ w&=\cos(\delta)\ \sin(ha) \end{aligned} \tag{2.16}$$

where

$$ha = sidereal\ time - \alpha \tag{2.17}$$

The transformation matrix, M_1 to the (east,north,up) Earth-based system is given by

$$M_1 = \begin{vmatrix} 1 & 0 & 0 \\ \cos(lat) & -\sin(lat) & 0 \\ \sin(lat) & \cos(lat) & 0 \end{vmatrix} \tag{2.18}$$

where *lat* is the latitude of the system mid-point.

Similarly the transformation, M_2, from the standard Earth-based system to the system aligned with the forward-scatter circuit is given by

$$M_2 = \begin{vmatrix} 0 & \cos(az) & \sin(az) \\ 0 & \sin(az) & -\cos(az) \\ 1 & 0 & 0 \end{vmatrix} \tag{2.19}$$

where *az* is the azimuth (° east of north) of the transmitter-receiver line.

The next task is to choose a distribution of meteor radiants which will allow us to predict the observed echo-rates and in the next section we review much of the previous work in this area and present the results of analysis of the most important meteor orbit surveys which have recently been made easily accessible in digital form.

2.2 Sporadic meteor radiant distributions from orbital surveys.

Apart from the early theoretical work of Schiaparelli (1866), and Von Niessl (1878) and the observational work on visual meteors by Denning (1886) and Hoffmeister (1948), one of the most important recent studies of the distribution of the radiants of sporadic meteors is that of Hawkins(1956). He found that sporadic radiants were concentrated in the ecliptic plane in three principle sources; an apex source, an anti-helion component and a helion source. This picture was supported by visual observations showing strong anti-helion and Apex sporadic sources (Hawkins and Prentice, 1957). Hawkins' work still forms the basis for almost all work done on sporadic distributions to this day. Extensive discussion of the nature of these sources can be found in the work of Davies (1957).

Hawkins' model which had been constructed using observations from the northern hemisphere was extended by Weiss and Smith (1960) using radio-meteor data gathered in Australia. They confirmed Hawkins' picture detecting three principle sporadic sources at the apex, anti-helion and helion points. Keay (1963) confirmed that this three source picture adequately explained the diurnal rate variations detected by the radar system in Adelaide and suggested their relative strengths be 2:1:2 for the helion, apex, and anti-helion sources respectively. Moreover, he noted that the strength of the sources varied widely during the year, confirming the earlier conclusions of Davies and Gill (1960) from a study of faint sporadic meteor orbits.

Stohl (1968), after analyzing data from the Springhill Meteor Radar in Canada extended this model to include a fourth source which he calls the "toroidal source" located at ecliptic latitude $+60°$ with the same Sun-centred longitude as the apex source. This four source picture has persisted to the present day, though the simple three source model of Hawkins is also still used.

It is important to be able to describe the sporadic radiant distribution accurately to obtain reliable predictions of the performance of forward-scatter meteor burst communication systems (Meeks and James,1959; Weitzen, 1986).

Both Davies (1957) and Hawkins (1956) studies use data from one of the earliest meteor radars at Jodrell bank. Since this time there have been numerous large radar surveys such as the Harvard Radio Survey (Sekanina, 1976), and additional photographic data such as the work of McCrosky and Posen (1963). The raw data from all these surveys has recently become available through the IAU Meteor Data Center in Lund, Sweden (Lindblad, 1987). The present work uses data available from the IAUMDC to determine the significant sporadic sources on the celestial sphere. In this section we investigate the widths and positions of the sources to bring the pioneering work of Hawkins up to date and re-evaluate the spatial distribution of sporadic meteors.

2.2.1 The survey data.

Ten surveys were selected form the IAUMDC to study the sporadic complex. Details of each survey are presented in table 1. The orbital data from the surveys was used to filter out major meteor showers which might interfere with the sporadic background, particularly for the relatively small photographic surveys. To do this, the stream elements for the showers listed in table 2 were used and each orbit in all surveys compared with these mean stream orbits. The shower members were removed on the basis of Hawkins and Southworth's D criterion which is a measure of orbital similarity such that identical orbits have a D coefficient of zero. Porubcan has found that a convenient measure of stream membership is whether the D value for an orbit with respect to the mean stream orbit is less than 0.5 and we have therefore excluded those meteors from our study for which D was in this range for any of the major showers. The remaining meteors in each survey then had their radiant points converted to a point on the celestial sphere in the Hammer-Aitoff equal area projection. To define contours on these maps, the celestial sphere was broken up into $5° \times 5°$ degree squares and meteors in each of these regions counted. The relative radiant density in each area is then compared using contours plots.

2.2.2 Results.

The final distribution for some selected surveys is given in figures 2.9a-d which are from the perspective of an observer looking towards the apex. The coordinates are expressed in terms of a Sun-centred longitude ($L = \lambda - \lambda_{\odot}$), and ecliptic latitude (β). Inspection of these activity profiles reveals immediately that there are several major sporadic sources common to these surveys. The anti-helion (AH) activity source is prominent in all surveys, occurring close to Sun-centred longitude ~ 190° and ecliptic latitude 0° . The "partner" source to this is the helion (H) source visible in all the radar surveys (though it is not present in the photographic data which is necessarily gathered during the hours of darkness) at longitude ~ 345° and 0° ecliptic latitude. The other two clearly visible radar sources are the north toroidal (NT) source located near 270° longitude and +60° latitude and its partner source the south toroidal (ST) component located near 270° longitude and -60° latitude. In addition, several northern radar surveys clearly show a "north" apex (NA) source at 270° longitude and +20° latitude which are also weakly discernable on some photographic surveys. The partner source of this is the south apex (SA) source, which is weakly visible in some northern radar surveys and somewhat clearer in the Adelaide work. Unfortunately, the Adelaide surveys were relatively small and so the numbers involved leave the physical character of the SA source open to question.

Table III - Characteristics of sporadic sources. Radii in degrees, long is sun-centred and latitude is ecliptic latitude.

Survey	Data		AH	H	NA	SA	NT	ST
	radii	25	20	23	-	23	-	
Harvard I	strength		.58	.35	.46	.18	1	-
	long	199	341	269	275	273	-	
	lat	3	2	28	-11	59	-	
	radii	18	19	22	-	18	-	
Harvard II	strength		.37	.20	.35	.10	1	-
	long	199	341	270	270	274	-	
	lat	2	2	25	-15	59	-	
	radii	16	15	-	-	-	17	
Adelaide I	strength		1	.57	.14	.24	-	.33
	long	193	345	273	272,	-	267	
	lat	-4	0	11	-15	-	-59	
	radii	14	10	-	-	-	15	
Adelaide II	strength		1	.44	.47	.44	-	.63
	long	195	344	272	273	-	280	
	lat	-5	0	7	-6	-	-60	
	radii		17	16	15	-	17	-
Kharkov	strength	.33	.27	1	-	.53	-	
	long	201	341	272	-	267	-	
	lat	5	3	20	-	55	-	
	radii	15	-	8	-	-	-	
Fireball	strength		1	-	.14	-	-	-
	long	184	-	273	-	-	-	
	lat	-2	-	12	-	-	-	

Table II - Meteor streams and their associated orbital elements filtered out of the surveys. Here ϖ is the argument of perihelion in degrees, e is the orbital eccentricity, q is the perihelion distance in a.u., i is the inclination and Ω is the longitude of the ascending node (1950.0).

Stream	ϖ	e	q	i	Ω
Perseids	151.5	0.965	0.953	113.8	139
Geminids	324.3	0.896	0.142	23.6	261
Orionids	82.5	0.962	0.571	163.9	28
Arietids	29	0.94	0.09	21	77
Quadrantids	170	0.683	0.977	72.5	282.7
Delta Aquarids	152.8	0.976	0.069	27.2	305

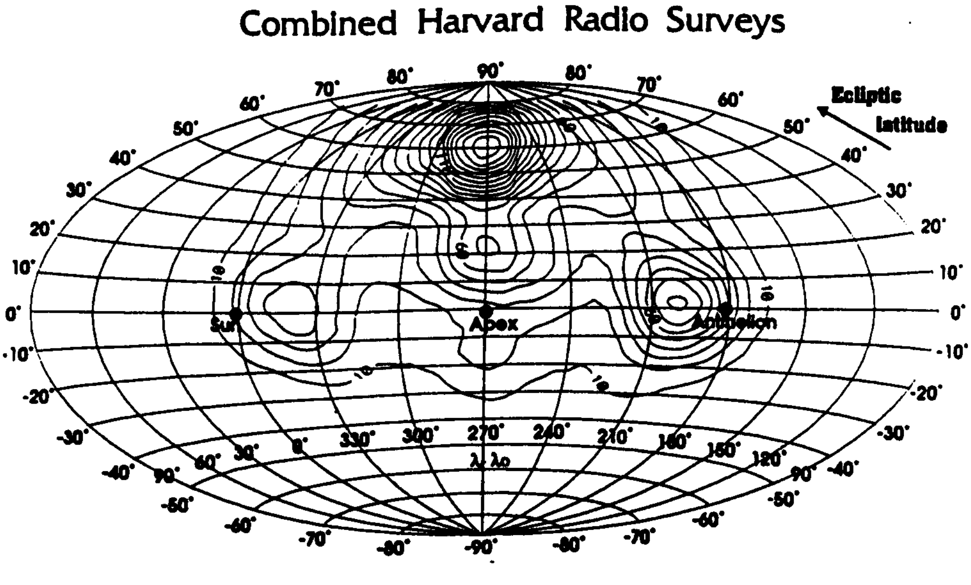

Figure 2.9a

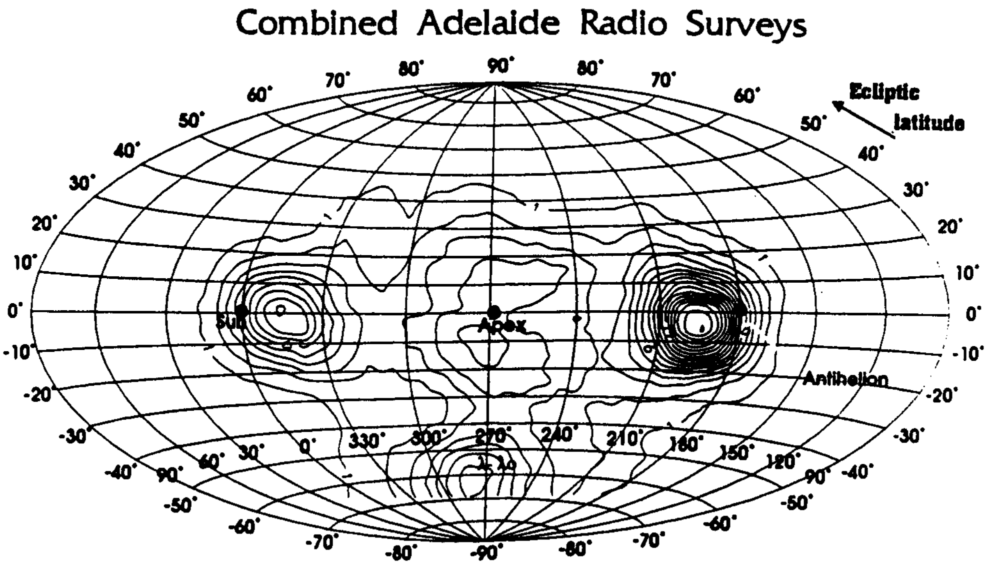

Figure 2.9b

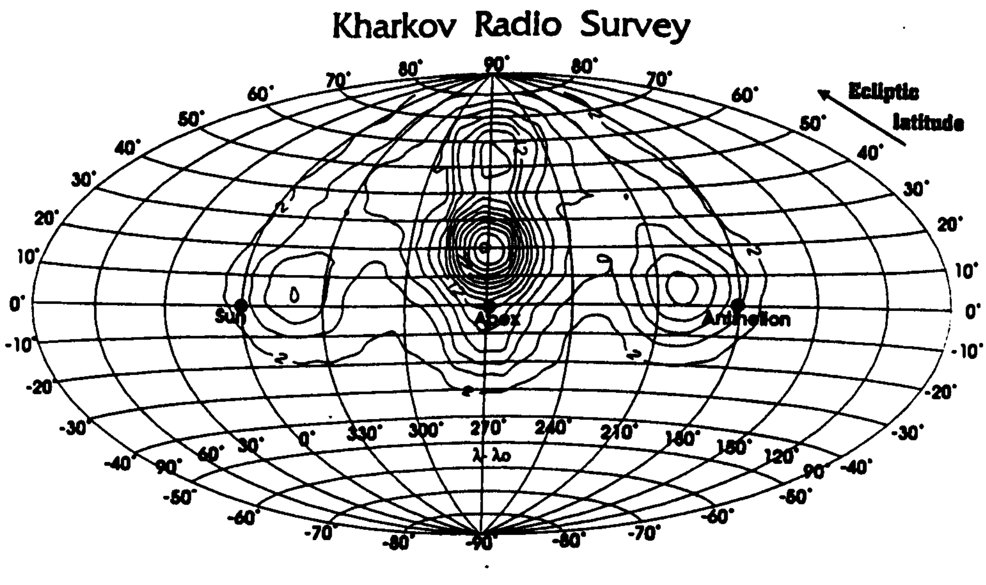

Figure 2.9c

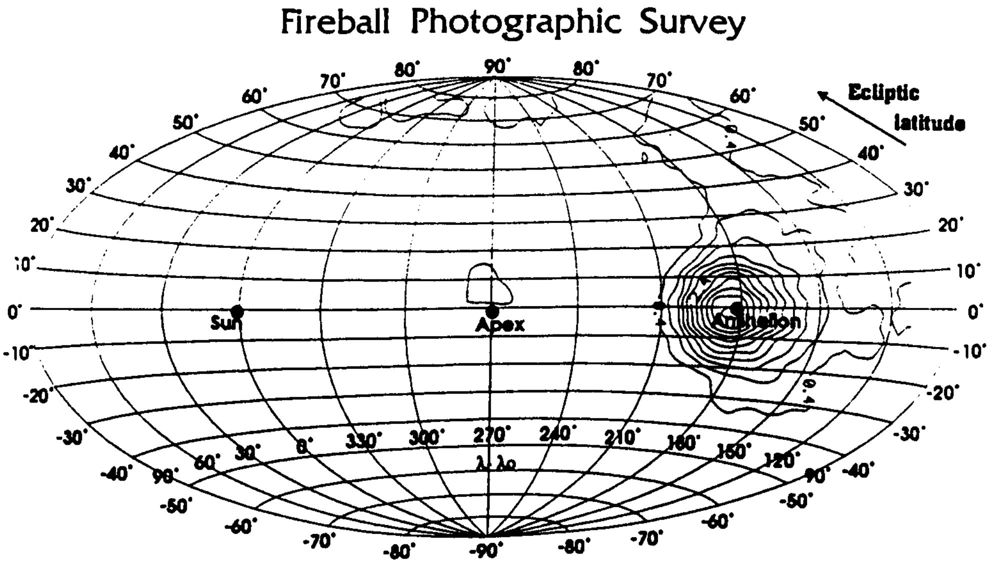

Figure 2.9d

For all the surveys, the centre of each of these sources, if visible, was measured and their full width at half-maximum (FWHM) in all the cardinal directions determined in angular terms. In Table III the mean radii of each source (found from the average of each FWHM measurement), and its position in each survey is given. In addition the relative strengths of each source, normalized to the strongest source within a given survey are presented.

The source strengths vary widely from survey to survey. In addition the position and visibility of each sporadic source is somewhat different between surveys. This is most likely the result of the complete lack of uniform corrections applied to all the data, such as a velocity correction in the case of radar. Initial train radius is also a significant cause of bias in the estimate of the source strengths for the radar surveys as is angular velocity for the photographic surveys. This may explain, in part, why the apex sources are in general rather weak compared with the other sources. It should be noted that for unknown reasons, all orbits with southern ecliptic latitude radiants were excluded from the Obninsk survey before it was released to the IAUMDC. All data used was exactly as given in the IAUMDC.

The widths of the sources vary for numerous selection reasons and there might also be an intrinsic mass dependence. For example the photographic source widths appear smaller than the radar widths as would be expected since the smaller radar particles will be influenced much more strongly by radiation forces than the larger photographic particles as a result of their larger surface area to mass ratio.

In spite of the differences in observation systems and locations there is much agreement between the surveys. The placement of the source positions is roughly the same (within the 2°-3° accuracy of the grid smoothing used) and the existence of six major sources is established.

2.2.3 Application of the orbit survey results to forward-scatter system.

Although the survey described above gives us a good idea of the positions and widths of the various sources, their apparent strengths are determined to a large extent by the geometry of the particular radars used in the survey so that their intrinsic strengths are still unknown. In this section we have developed a method by which the strengths of the sources can be found from the echo rates measured with the Ottawa-Elginfield system. The total observed rate, Ξ_{tot}, is given by

$$\Xi_{tot}=\Sigma\ a_i\ \Xi_i \tag{2.20}$$

where Ξ_i is the rate due to the i'th source (assumed to be of unit strength) and a_i is the weight of that source.

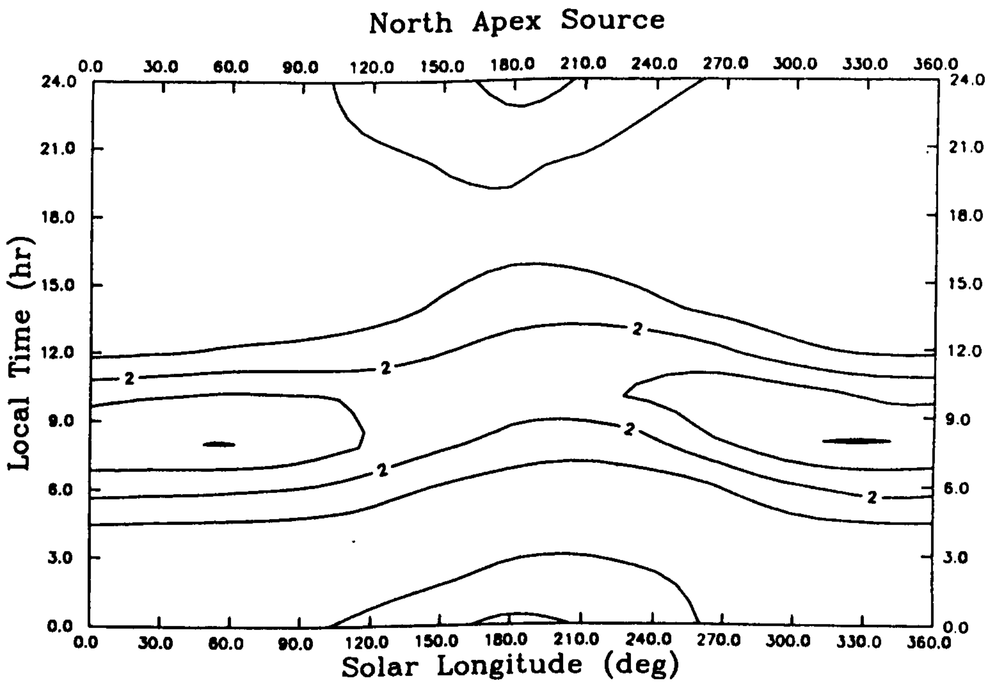

Figure 2.10 a

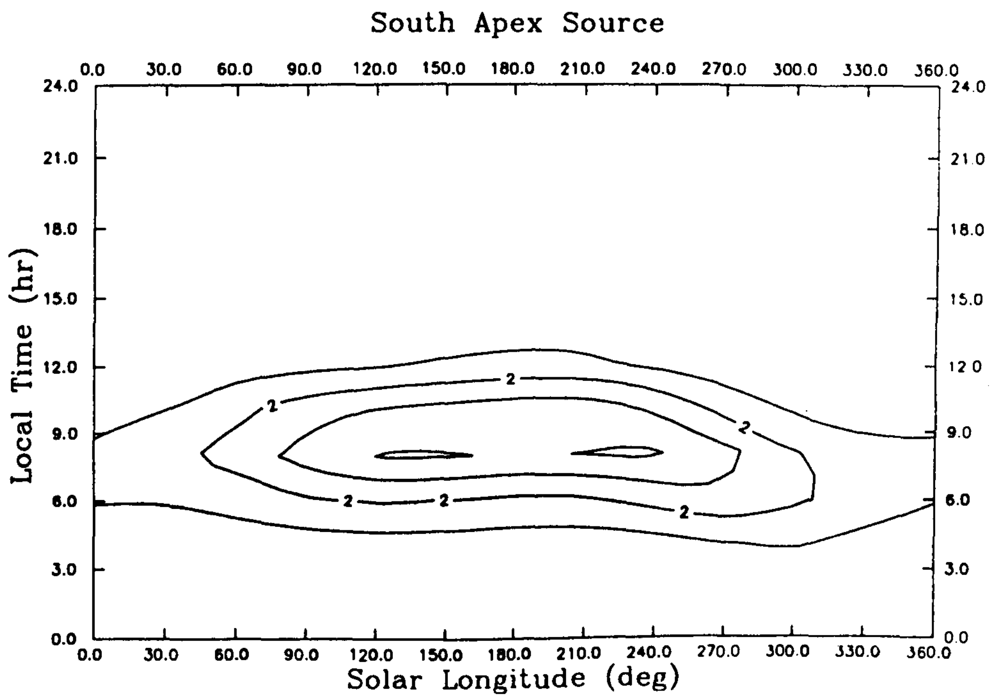

Figure 2.10 b

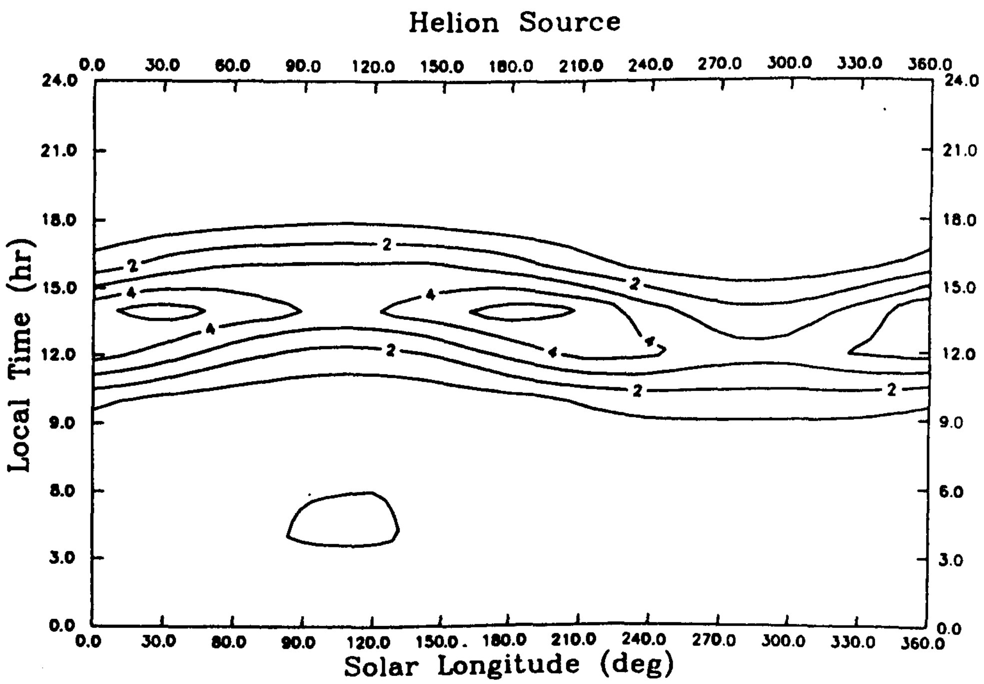

Figure 2.10 c

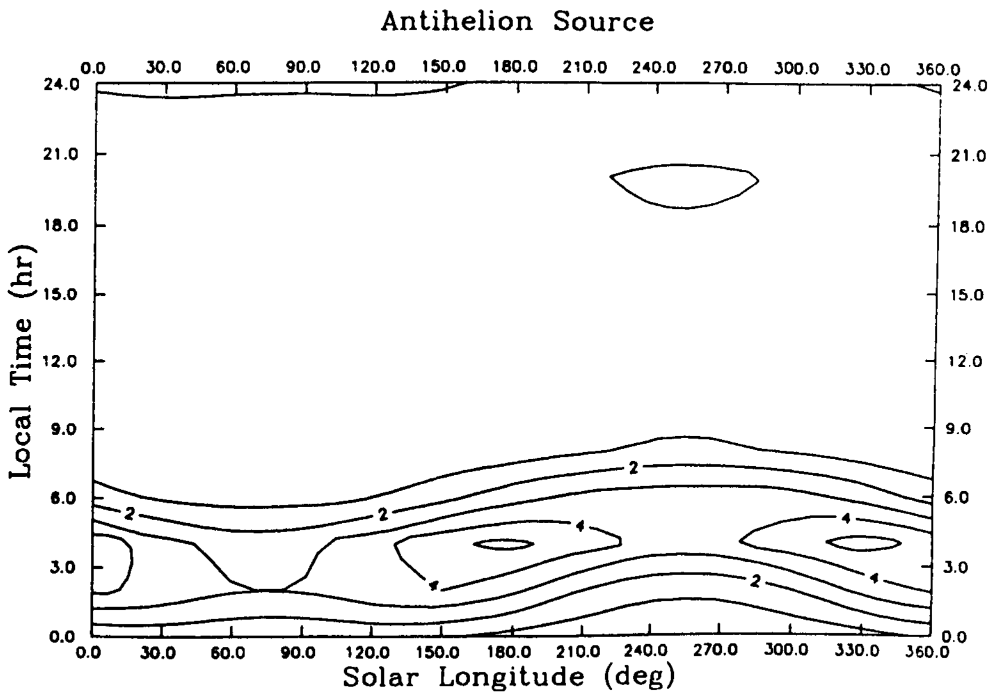

Figure 2.10 d

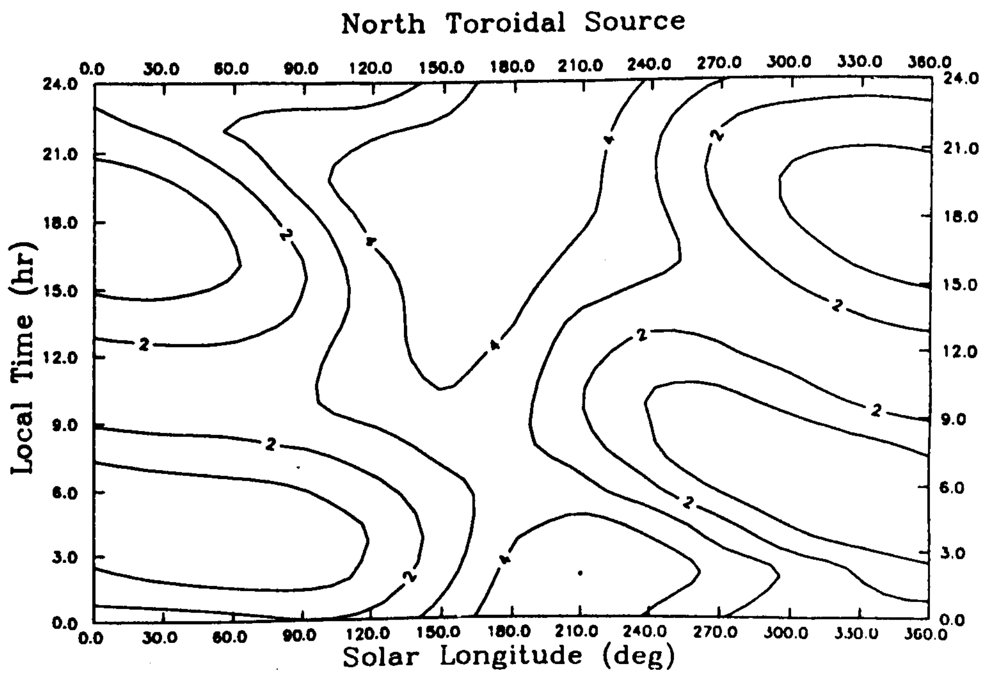

Figure 2.10 e.

Smoothed observed echo rates

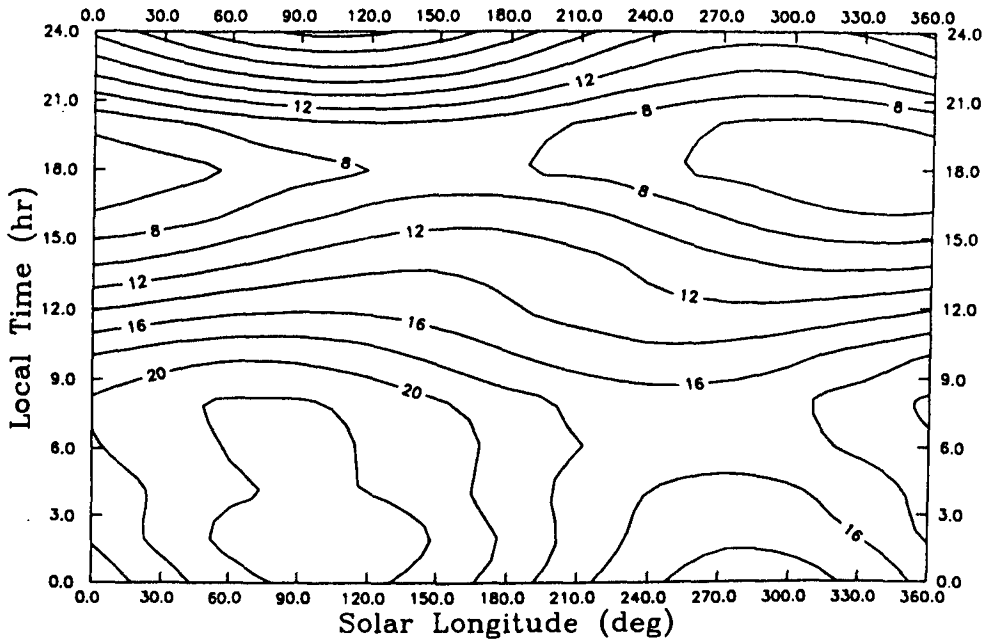

Figure 2.11. Observed echo rates

Predicted echo rates with several sources

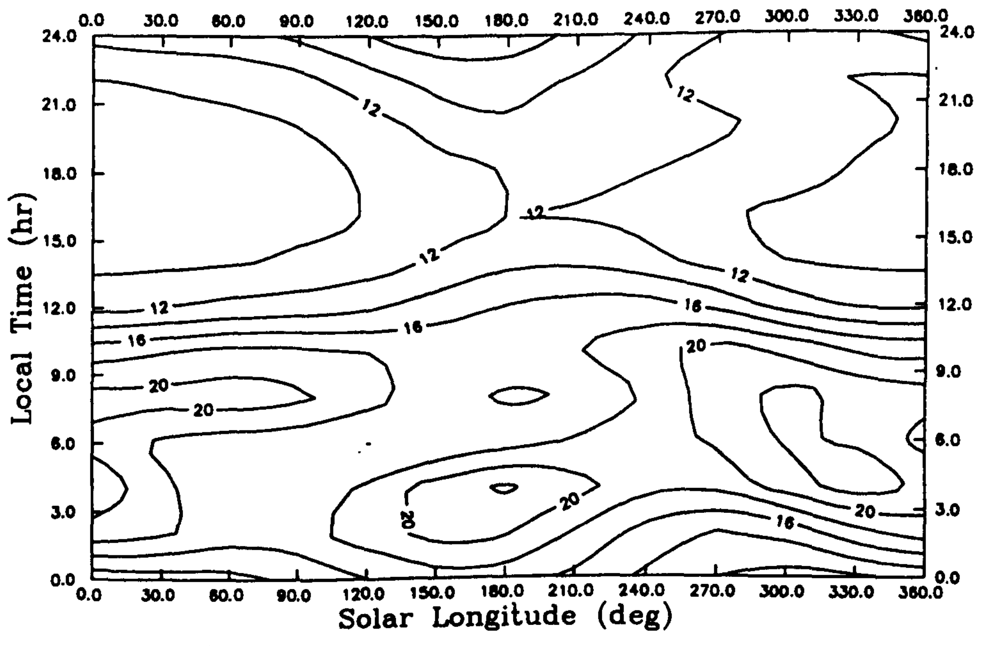

Figure 2.12. Predicted echo rates with background = 8.8, N. Apex = 2.7, S. Apex = 0.3, Helion = 0.0, Antihelion= 2.2, N. Toroidal = 0.3.

The functions Ξ_i were calculated for each source using a Monte-Carlo simulation in which 400 radiants generated according to the radiant distribution of each source were used to calculated the average response of the system to that particular source for each hour throughout the day and for 12 equally spaced intervals throughout the year and the results of these calculations are shown in figures 2.10a-e. No calculations were performed for the South Toroidal source since meteors from it are not visible in the northern hemisphere. The remaining task is to choose the coefficients a_i in order to obtain a good fit with the observed data which is shown in similar format in figure 2.11 while figure 2.12 shows a theoretical prediction with a particular choice of values for a_i.

2.3 Summary

We have developed a method for predicting the response of any forward-scatter system to any distribution of radiants. Since the distribution of sporadic radiants is not well known we have made an analysis of the major surveys of meteors orbits and found that there appear to be six major sources of sporadic meteor radiants. We have calculated the response of our forward-scatter system to each of these sources and the composite predicted echo rate (figure 2.12) compares favourably with the observed echo rate (figure 2.11). However this represents a first attempt and improved predictions are to be expected from further refinements. The next step will be to determine the relative strengths of each of the sporadic sources using a least-squares fitting procedure, recognizing that these source strengths are likely to have seasonal variations.

3. Impulse Response Measurements

3.1 Introduction

An important factor limiting the overall performance and consequently the usefulness of a meteor burst communication system, is the maximum data rate that can be supported by the channel. In the majority of cases, this rate is usually deduced from knowledge of the channel impulse response which is ultimately obtained using empirical techniques. To date however, little research has been undertaken, with the notable exception of that conducted by Weitzen et. al (1984, 1987) and a few others, to measure systematically the impulse response and to develop a model for the meteor burst communication channel. Because of the underlying value of this information, a measurement system employing a linear F.M. pulse compression (chirp) radar has been designed and is currently under construction. In addition to measuring the channel impulse response, this system will also permit measurements of path length, time-of-flight and their associated distributions. This additional information is valuable since it will provide insight into other important implementation related issues such as system synchronization. The remainder of this chapter details the operation and expected performance of the proposed measurement system.

3.2 Principles of operation

A simplified block diagram of the measurement system is shown in Figure 3.1. The signal emitted by the transmitter is a linear F.M. waveform (chirp) and is described by the equation:

$$s(t) = p(t)\cos\left(2\pi f_o t + \pi\mu t^2\right) \ , \qquad (3.1)$$

where; f_o is the starting frequency of the chirp (Hz), μ is the chirp rate (Hz/sec.) and $p(t)$ is a unipolar rectangular switching waveform which controls the duration and repetition rate of the transmitted signal. The chirp signal generated at the receiver is similar to that generated at the transmitter and is described by:

$$c(t) = p_1(t - T_d)\cos\left(2\pi(f_o + f_d - \mu T_d)t + \pi\mu t^2 + \theta\right) \ , \qquad (3.2)$$

where; f_d is the frequency offset (Hz), T_d (sec.) is the delay between the starting times of the chirp waveforms generated at the transmitter and the receiver, θ is the phase angle (rad.) and all other symbols have their usual meanings. When the signal emitted by the transmitter arrives at the receiver after having been delayed by the flight-time, T_p , it is mixed with the locally generated chirp, $c(t)$, and produces the receiver output signal, $d(t)$, given by:

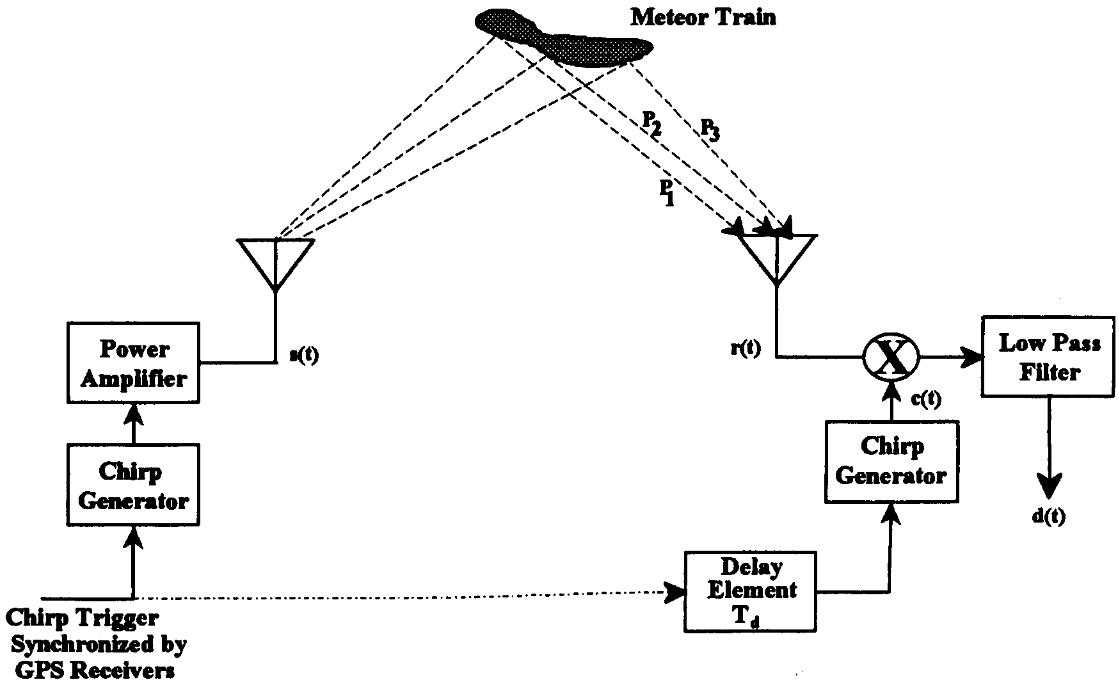

Figure 3.1: Simplified Block Diagram of the Measurement System

$$d(t) = \sum_{k=1}^{N} \beta_k \, p(t - T_{pk}) \cos\left(2\pi\left(f_d + \mu\left(T_{pk} - T_d\right)\right)t + \theta_1\right) \ , \tag{3.3}$$

where; N is the number of paths between the transmitter and receiver, β_k and T_{pk} represent the attenuation and flight-times for the k^{th} path and all other parameters have their usual meanings. All measurements of interest (time-of-flight etc.) are derived from the amplitude spectrum of *d(t)*. A sketch of a typical spectrum is shown in Figure 3.2. for the case in which 3 paths exist between transmitter and receiver. In this case, the flight-times for each path are estimated from knowledge of the frequency components, f_k, the system parameters μ, f_d and T_d and the equation:

$$T_{pk} = T_d + \frac{f_k - f_d}{\mu} \ . \tag{3.4}$$

It should be noted that knowledge of *Td* requires that the transmitter and receiver timing be synchronized and this is accomplished through the use of Global Positioning Satellite (GPS) receivers located at both ends of the link. Having obtained the flight-times, the corresponding path lengths, P_k, can be computed using:

$$P_k = c \, T_{pk} \ , \tag{3.5}$$

where c is the velocity of light in a vacuum. In addition to providing time-of-flight information, the amplitude spectrum of *d(t)* represents the impulse response of the channel and can be used in conjunction with the Fourier transform to estimate the channel transfer function.

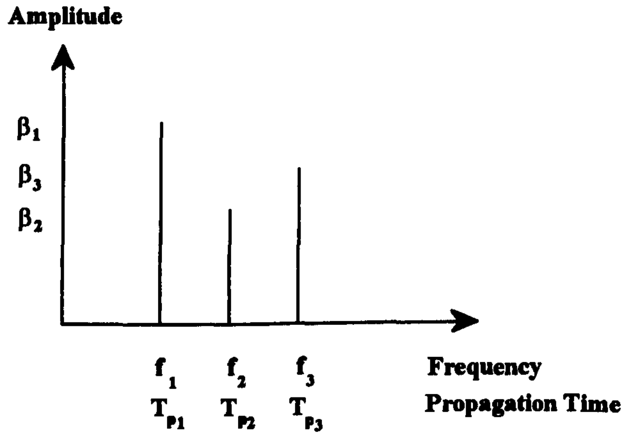

Figure 3.2: Impulse Response of Multipath Channel

3.3 System operation

The measurement system has been designed to collect data on both a continuous and triggered basis. In the continuous mode of operation, the receiver output is recorded continuously on video tape for a period of several hours. The disadvantages of this approach are that portions of the tape will contain no useful information during the absence of suitably ionized trains and that the entire tape must processed to determine if any ionized trains were present. The attractive feature of this mode is that a permanent record of the signal is always available and can be scrutinized for weak signals using digital signal processing techniques. In the triggered mode of operation the system records data only when trains having suitable ionization are present. This is accomplished by transmitting a 10 ms carrier, or "probe" signal, 20 ms in advance of the chirp transmission. When the "probe" signal is detected by the receiver, its output is digitized and stored in a convenient form. A diagram showing the transmission cycle is given Figure 3.3. Regardless of the recording mode, repetitive transmission of the chirp signal at intervals of 100 ms permit variations in the channel characteristics to be recorded over the duration of the burst. For typical durations of 1.0 second, approximately 10 measurements can be obtained.

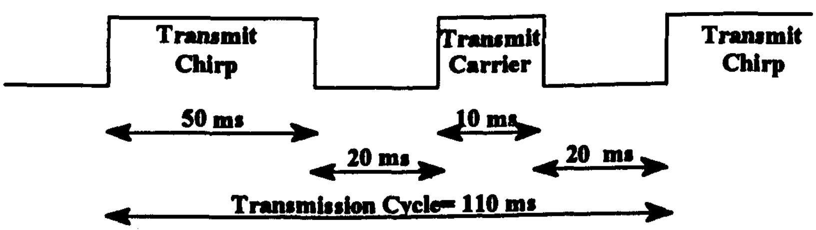

Figure 3.3: Transmission Cycle

3.4 Signal-to-noise ratio

To ensure a 90% detection probability, a signal-to-noise ratio (SNR) of between 20 and 30 dB is required. In the case of matched filter detection, the SNR is given by:

$$SNR = \frac{2E_g}{N_o} , \tag{3.6}$$

where; E_g is the received signal energy and N_O is the noise power spectral density (measured 4×10^{-17} Watts/Hz). Following the analysis of Chow (1992), the received energy, E_g is given by:

$$E_g = \frac{P_T G_T G_R \lambda^3 q^2 r_e^2}{16\pi^2 R_T R_R (R_T + R_R)} \tau , \tag{3.7}$$

where; P_T is the transmitter power (1.0 kW), G_T and G_R are the antenna gains (5 dB), λ is the free space wavelength (7.5 m), q is the electron line density in electrons per meter (1.0 $\times10^{14}$), r_e is the classical electron radius (2.8178×10^{-15} m), R_T and R_R are the distances from the transmitter and receiver to the point of tangency at the train (250 km for the Ottawa/London link) and τ is the chirp duration (50 ms). Assuming the values quoted above, a SNR of approximately 22 dB is obtained and is sufficient to ensure reliable detection.

3.5 Resolution

The resolution of the measurement system is proportional to the chirp bandwidth. For this system, the chirp bandwidth is 2.5 MHz and consequently flight-times differing by 400 ns (a path length differential of 120 m) can be resolved.

3.6 The transmitter

For ease of presentation the block diagram of the transmitter has been divided into three sections: the composite signal generator, the up-converter and the power amplifier section. The following paragraphs briefly outline the function and operation of each of these sections. Where possible, the expected signal levels, attenuation and filter cutoff frequencies have been included in the diagrams.

The purpose of the composite signal generator (see Figure 3.4) is to combine the chirp and carrier signals to produce a composite signal which, when applied to the up-converter, will result in an output signal having the desired spectrum. As indicated in the diagram, the chirp generator produces a baseband signal having the characteristics listed in Table 3.1. Chirp transmission is initiated on the rising **edge** of the trigger signal.

Table 3.1: Chirp Characteristics

Starting Frequency:	1.0 MHz
Stopping Frequency:	3.5 MHz
Bandwidth:	2.5 MHz
Duration:	50.0 ms
Chirp Rate (μ):	5.0×10^7 Hz/sec.

The carrier or "probe" signal is generated through the use of a stable 5.0 MHz oscillator and is controlled by the level applied to the carrier transmit control line. The duration of the probe signal is 10 ms as indicated previously in Figure 3.3.

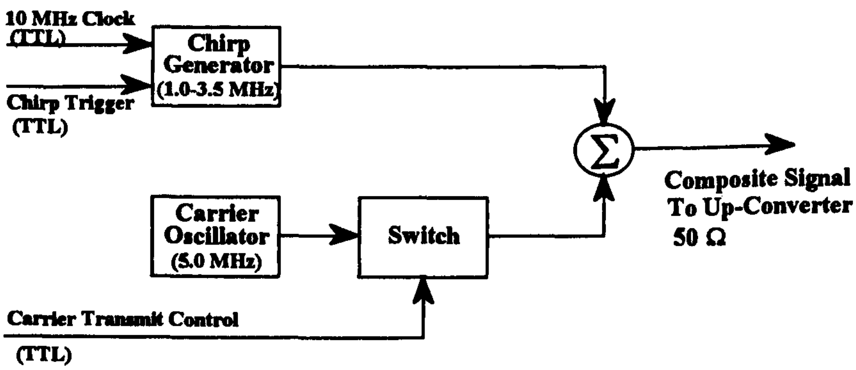

Figure 3.4: Composite Signal Generator

Since the signal produced by the composite signal generator is a baseband signal, it must be translated in order to obtain the desired spectrum. The up-converter of Figure 3.5 translates the spectrum and produces a chirp signal having starting and stopping frequencies of 38.75 and 41.25 MHz and a carrier signal at 42.75 MHz. Band pass filters are used after each translation in order to attenuate unwanted sidebands and spurious high frequency components which may be present in the system.

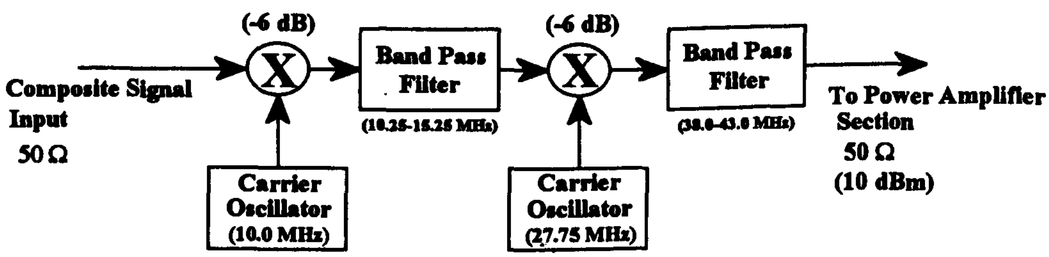

Figure 3.5: Up-Converter

Following the up-conversion process, the signal must be amplified to a suitable level for transmission. The power amplifier section shown in Figure 3.6 amplifies the signal from the up-converter from a level of 10 dBm to approximately 60 dBm (1.0 kW).

As in the up-converter section, band pass filters are required to attenuate unwanted frequency components occurring outside the desired passband from 38.0 to 43.0 MHz. The output signal from this section is then fed to the antenna.

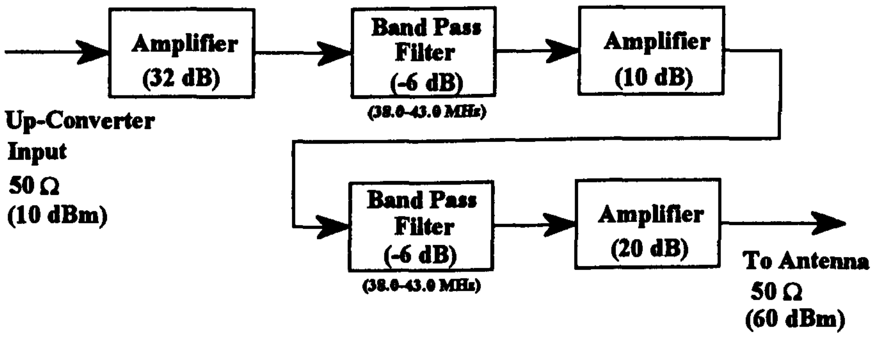

Figure 3.6: Power Amplifier Section

3.7 The receiver

As in the previous section, the block diagram of the receiver has been divided into sections for ease of presentation. These are: the carrier detector/down-converter section, the I.F. section and the data storage section. The function and operation of each of these sections is outlined briefly in the following paragraphs. As in the discussion of the transmitter, signal levels, attenuation and filter cutoff frequencies have been included in the diagrams wherever possible.

The carrier detector/down-converter section serves two functions. The first is to detect the presence of the carrier or "probe" signal at 42.75 MHz and the second is to translate the spectrum of the chirp to baseband for demodulation and recording by the I.F. and data storage sections. A block diagram of the carrier/down-converter section can be found in Figure 3.7. When the carrier signal is present, it is amplified and demodulated by the VHF receiver and carrier detect circuitry. If the signal level is sufficiently strong the carrier detect circuitry generates a pulse which triggers the A/D converter and its associated data recording system. When the chirp signal is present, it is applied to the down-converter and translated to baseband as previously indicated. The starting and stopping frequencies of the chirp at this point are identical to those of the transmitted chirp and are 1.0 and 3.5 MHz respectively.

When the I.F. signal is mixed with the locally generated chirp and filtered as shown in Figure 3.8, beats are produced as discussed in Section 3.2. It should be noted that the starting and stopping frequencies of the local chirp are offset from those of the transmitter by 12 kHz as indicated in the diagram. At this point in the receiver, the signal path is split and applied to both the A/D converter and quadrature detection circuits. Signals applied to the A/D converter are recorded only when triggered by the "probe" signal while those applied to the quadrature detector are recorded continuously. Quadrature detection is necessary in this system to permit the spectrum of the demodulated signal, which has a bandwidth of approximately 50 kHz, to be recorded on the two 25 kHz audio channels of the data recording unit.

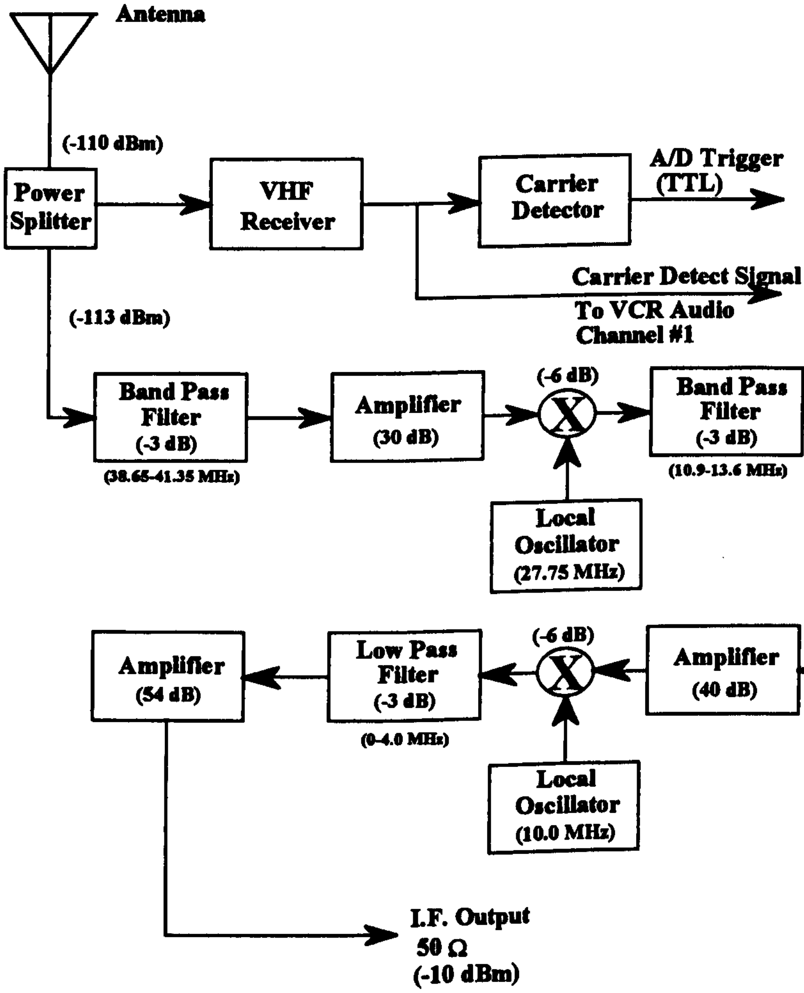

Figure 3.7: Carrier Detector /Down-Converter Section

A block diagram of the data recording and storage section is shown in Figure 3.9. The analog signal from the I.F. section is applied to the A/D converter, sampled at a rate of approximately 150 kHz and stored in binary format on tape. In-phase and quadrature signals are applied to the SONY digital audio processor which generates a composite signal and is stored on the video channel of the VCR. Audio signals containing timing information are recorded on the audio tracks of the video tape so that timing information can be used to index portions of the recording. Two sources of timing information are recorded - an audio time signal received from the time station CHU and the 1.0 kHz time signal from the GPS receiver.

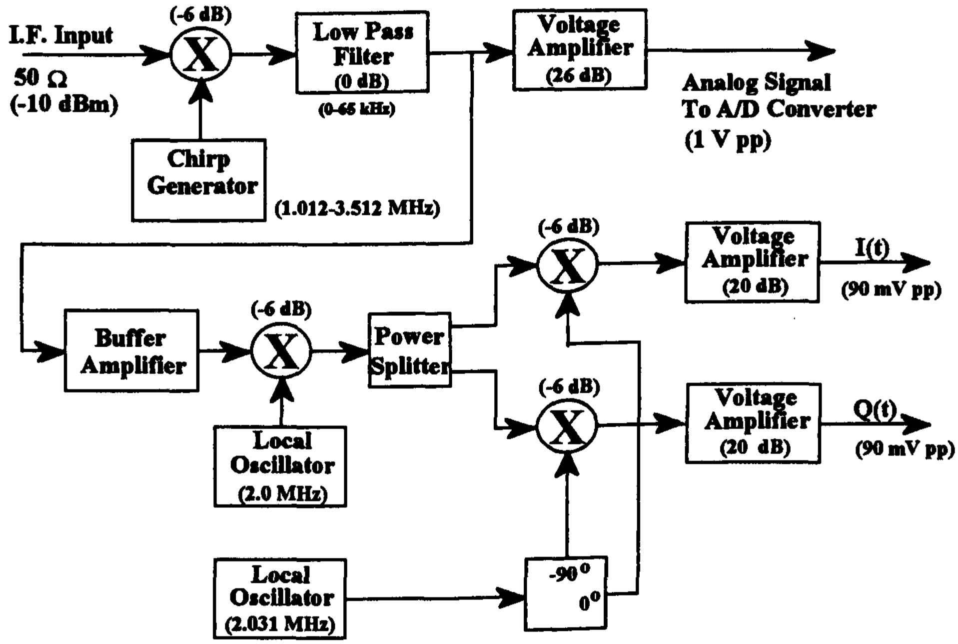

Figure 3.8: I.F. Section

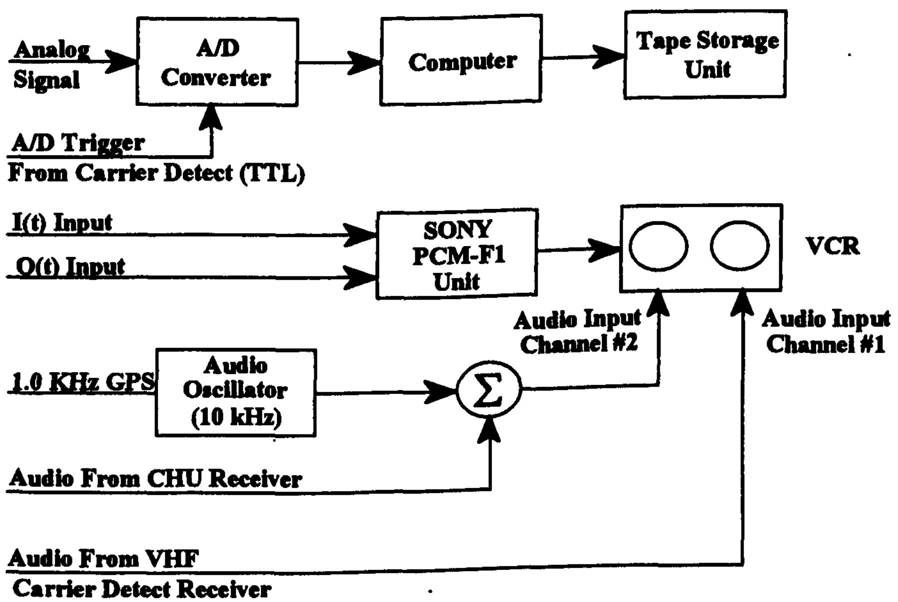

Figure 3.9: Data Recording and Storage

3.8 Concluding remarks

Research to date has been aimed primarily at the development of the measurement system described in the preceding sections. At present, the majority of the design work has been completed and work has begun on construction of the apparatus. It is expected that this work will be completed by June 1993. Once construction of the measurement system has been completed, it is planned that its operation will be verified in both laboratory and field trials. Trials conducted in the laboratory will be used to ensure that the system satisfies the design requirements and will also provide the opportunity to test and debug the signal processing/data analysis software. Field trials will begin upon completion of the laboratory testing and will be used to obtain preliminary data on the channel characteristics. At the conclusion of these trials, the transmitter and receiver for the measurement system will be installed at the Ottawa/Elginfield sites currently housing the interferometer equipment. Relocation of the apparatus in this manner will enable time-of-flight measurements to be correlated with similar measures obtained using the interferometer.

4. References

Chow, S., 1992, Personal Communication, Communications Research Centre, Shirley's Bay, Ottawa, Ontario.

Davies, J.G., 1957, Adv. in Electronics and Elect. Phys., **9**, 95.

Flemming, D.B.E, Hawkes, R.L. and Jones, J. 1992, Proc. IAS Symposium *"Meteors and their parent bodies"*, Smolenice, Slovakia.

Hawkins, G.S., 1956, Ast., J., **61**, 386.

Hawkins, G.S., 1956, Mon. Not. R. astr. Soc., **116**, 92.

Hawkins, G.S, and Prentice, J.P.M., Ast. J., **62**, 234.

Hines, C.O. 1955, Can. J. Phys. **33**, 600

Hines, C.O. 1958, Can J. Phys. **36,** 117.

Hoffmeister, C., *Meteorstrome*, 1948.

Kaiser, T.R. 1960, Mon. Not. R. astr. Soc., **121**, 284.

Keay,C.S.L. 1963, Mon. Not. R. astr. Soc. **25**, 507.

Lindblad, B.A., 1987, Pub. Astr. Inst. Czec., **67**, 201.

McCrosky, R.C., Posen, A., Smithson. Contr. astrophys., **4**, 15.

McKinley, D.W.R., 1961, In *Meteor Science and Engineering*, McGraw-Hill, New York.

Meeks, M. L., and James, J. C., 1959, JATP, **16**, 228.

Schiaparelli, G.V., 1866, *Sternschnuppen*.

Sekanina, Z., 1976, Icarus, **27**, 265.

Stohl, J., 1968, In: *Physics and Dynamics of Meteors*, p. 298, eds. L. Kresak. and P.M. Millman. Reidel, Dordrecht, Holland.

von Niessl, 1878 , Astr. Nachr., **93**, 209.

Webster, A.R., Jones, J. and Ellis, K.J., 1992, D.S.S. Contract O55SS.36001-1-3522, Final Report.

Weiss, A.A., and Smith, J.W., 1960, Mon. Not. R. astr. Soc., **121**, 5.

Weitzen, J.A., Grossi, M.D., Birkemeier, W.P., 1984, Radio Science, Vol. 19, No.1, pp. 375-381.

Weitzen, J.A., Sowa, M.J., Scofidio, R.A., Quinn, J., 1987, IEEE Trans. on Communications, Vol. COM-35,No. 10, pp. 1050 -1058.

Weitzen, J.A., 1986, Radio Science, **21**, 1009.